Journal of Alloys and Compounds 522 (2012) 149–156

Contents lists available at SciVerse ScienceDirect

Journal of Alloys and Compounds

journal homepage: www.elsevier.com/locate/jallcom

Liquid–solid phase equilibria in Nb-rich corner of the Nb–Ti–Si–B system

Zhiping Sun [a], Xiping Guo [a,*], Chuan Zhang [b]

[a] State Key Laboratory of Solidification Processing, Northwestern Polytechnical University, Xi'an 710072, PR China
[b] CompuTherm, LLC, Madison, WI 53719, USA

ARTICLE INFO

Article history:
Received 14 November 2011
Received in revised form 18 January 2012
Accepted 23 January 2012
Available online 2 February 2012

Keywords:
High-temperature alloys
Intermetallics
Liquid–solid reactions
Phase diagrams
Microstructure

ABSTRACT

Nb–Ti–Si based alloys are considered as candidates of next-generation high temperature materials (i.e., working temperature >1200 °C). Boron has a beneficial effect in enhancing the oxidation resistance and reducing the anisotropy ratio a_c/a_a of the T2 phase in the Nb–Si alloys. The liquid–solid multiphase equilibria in the Nb–Ti–Si alloys with B additions have been investigated via an approach of integrating thermodynamic modeling with designed experiments. The present study suggests that Ti and Si additions increase the stability of Nb_3B_2, and the primary region of Nb_3B_2 will appear in the Nb–Ti–Si–B quaternary, while there is no primary solidification region of Nb_3B_2 in the constitute binaries and ternaries. The proposed liquidus surface of the Nb-rich Nb–Ti–Si–B system is associated with eight primary solidification regions of Nbss, T2, T1, $D8_8$, $(Nb,Ti)_3Si$, NbB, TiB and Nb_3B_2. The direct eutectic solidification occurs between Nbss and T2 in the Nb-rich region in the Nb–Ti–Si–B liquidus projection, which could provide new opportunities for alloy design based on the Nb–Ti–Si–B system.

© 2012 Elsevier B.V. All rights reserved.

1. Introduction

The development of in situ composites based on Nb solid solution (Nbss) and Nb_3Si/Nb_5Si_3 silicides has been motivated by the demand for high-temperature structural applications beyond those of Ni-based superalloys [1,2]. Ti, beneficial to both the oxidation resistance and room temperature fracture toughness, is one of the major alloying elements for the Nb–Si alloys [2,3]. Recently, it has been found that as a substitute for Si in the α-Nb_5(**Si**,B)$_3$ phase (to be referred as T2 afterwards), B has a beneficial effect in enhancing the oxidation resistance and reducing the anisotropy ratio a_c/a_a of T2 in the Nb–Si alloys [4,5]. In order to improve the design of new engineering materials and understand the relationship between microstructure and properties, the knowledge of the phase equilibria of the Nb–Ti–Si–B quaternary system is prerequisite. Detail information on the phase equilibria at 1500 °C in the Nb-rich region of the Nb–Ti–Si–B system has been reported elsewhere [6]. The objective of this study is to understand the effect of B addition on the liquid–solid phase equilibria in the Nb-rich Nb–Ti–Si–B alloys. This knowledge is essential to understand the microstructure and property of these Nb–Si alloys generated by liquid–solid processing techniques [7–9].

The strategy for establishing multicomponent phase equilibria in this study is experimental investigations coupled with thermodynamic modeling using the CALPHAD approach [10,11]. This work started with previously developed thermodynamic descriptions of the Nb–Si–B [12], Nb–Ti–Si [13], Nb–Ti–B [14] and Ti–Si–B [15] systems. Then, based on thermodynamic descriptions of the four constituent ternaries, Gibbs energy functions of the phases in the Nb–Ti–Si–B quaternary were obtained through the interpolation, and then isothermal section at 1500 °C and liquidus projection of the quaternary were calculated from these functions. Next, seven alloy compositions were selected for experimental investigation. These selected alloys were fabricated by arc-melting and heat treated at 1500 °C for 150 h. Their as-cast and annealed microstructures were then characterized. Lastly, the experimental results obtained in this study were used to improve or validate the Gibbs energy functions obtained from extrapolation, until all experimental data can be satisfactorily reproduced by calculation.

2. Background on liquidus surface of the constituent ternaries

Fig. 1 shows the three constituent ternary liquidus projection near the Nb corner, which will be explained in detail below.

2.1. Nb–Si–B

The bottom face in Fig. 1 shows the calculated liquidus projection of the Nb–Si–B system by Sun et al. [12]. In the region with the Si and B concentrations up to 30 at.%, there are six primary solidification phases: Nbss, Nb_3Si, NbB, T1, T2 and $D8_8$. The notations of all phases are explained in Table 1. T2 extends its homogeneity range from α-Nb_5Si_3 into the Nb–Si–B

* Corresponding author. Tel.: +86 29 88494873; fax: +86 29 88494873.
E-mail address: xpguo@nwpu.edu.cn (X. Guo).

0925-8388/$ – see front matter © 2012 Elsevier B.V. All rights reserved.
doi:10.1016/j.jallcom.2012.01.142

Table 1
Primary solidification phases at the Nb-rich region of the Nb–Ti–Si–B system.

Phase symbol	Thermodynamic model	Pearson symbol	Phase description
Nb–Si–B			
Nbss	$(\mathbf{Nb},Si)_1(B,Va)_3$	cI2	Ternary solid solution with the bcc_A2 structure
Nb_3Si	Nb_3Si	tP32	Binary compound Nb_3Si
T1	$(\mathbf{Nb},Si)_5(Nb,\mathbf{Si})_3$	tI32	Binary compound β-Nb_5Si_3
T2	$Nb_5(\mathbf{Si},B)_3$	tI32	Ternary solid solution based on the low temperature form of α-Nb_5Si_3($D8_l$)
$D8_8$	$Nb_5(\mathbf{Si},B)_3(\mathbf{B},Va)_1$	hP16	Ternary solid solution
NbB	$Nb(\mathbf{B},Si)$	oC8	Ternary solid solution based on the NbB
Nb–Ti–Si			
Nbss	$(\mathbf{Nb},\mathbf{Ti},Si)_1(Va)_3$	cI2	Ternary solid solution with the bcc_A2 structure
$(Nb,Ti)_3Si$	$(\mathbf{Nb},\mathbf{Ti})_3Si$	tP32	Ternary solid solution based on the Nb_3Si and Ti_3Si
α-Nb_5Si_3/T2	$(\mathbf{Nb},Ti)_5Si_3$	tI32	Ternary solid solution based on the low temperature form of α-Nb_5Si_3($D8_l$)
β-Nb_5Si_3/T1	$(\mathbf{Nb},Ti)_5Si_3$	tI32	Ternary solid solution based on the high temperature form of β-Nb_5Si_3($D8_m$)
Ti_5Si_3/$D8_8$	$(Nb,\mathbf{Ti})_5Si_3$	hP16	Ternary solid solution based on the Ti_5Si_3($D8_8$)
Nb–Ti–B			
Nbss	$(\mathbf{Nb},\mathbf{Ti})_1(B,Va)_3$	cI2	Ternary solid solution with the bcc_A2 structure
NbB	$(\mathbf{Nb},Ti)B$	oC8	Ternary solid solution based on the NbB
TiB	$(Nb,\mathbf{Ti})B$	oP8	Ternary solid solution based on the TiB
Nb–Ti–Si–B			
Nbss	$(\mathbf{Nb},\mathbf{Ti},Si)_1(B,Va)_3$	cI2	Quaternary solid solution with the bcc_A2 structure
T2	$(\mathbf{Nb},Ti)_5(\mathbf{Si},B)_3$	tI32	Quaternary solid solution based on the low temperature form of α-Nb_5Si_3 ($D8_l$)
T1	$(\mathbf{Nb},Ti)_5Si_3$	tI32	Quaternary solid solution based on the high temperature form of β-Nb_5Si_3($D8_m$)
$D8_8$	$Nb_5(\mathbf{Si},B)_3(\mathbf{B},Va)_1$	hP16	Quaternary solid solution based on the Ti_5Si_3
$(Nb,Ti)_3Si$	$(\mathbf{Nb},\mathbf{Ti})_3Si$	tP32	Quaternary solid solution based on the Nb_3Si and Ti_3Si
NbB	$(\mathbf{Nb},Ti)B$	oC8	Quaternary solid solution based on the NbB
TiB	$(Nb,\mathbf{Ti})B$	oP8	Quaternary solid solution based on the TiB
Nb_3B_2	$(\mathbf{Nb},Ti)_3(Si,\mathbf{B})_2$	tP10	Quaternary solid solution based on the Nb_3B_2

ternary by substituting Si with B. $D8_8$ has a Mn_5Si_3-prototype hexagonal unit cell, and it is formed by small B atoms filling the interstitial sites. Five ternary invariant reactions on the liquidus projection were reported in the Nb-rich corner [12]: II_1: L + NbB → Nbss + T2 at 1986.5 °C; II_2: L + T1 → Nb_3Si + T2 at 1963.2 °C; II_3: L + Nb_3Si → Nbss + T2 at 1888.2 °C; III_1: L + NbB + $D8_8$ → T2 at 2174.8 °C; III_2: L + T1 + $D8_8$ → T2 at 2160.1 °C. In addition, two minimum points were proposed to occur on the L → Nbss + T2 and L + $D8_8$ → T2 monovariant lines, respectively. The calculated reaction types and primary solidification regions in Nb-rich corner are in accordance with those proposed by Junior et al. [16].

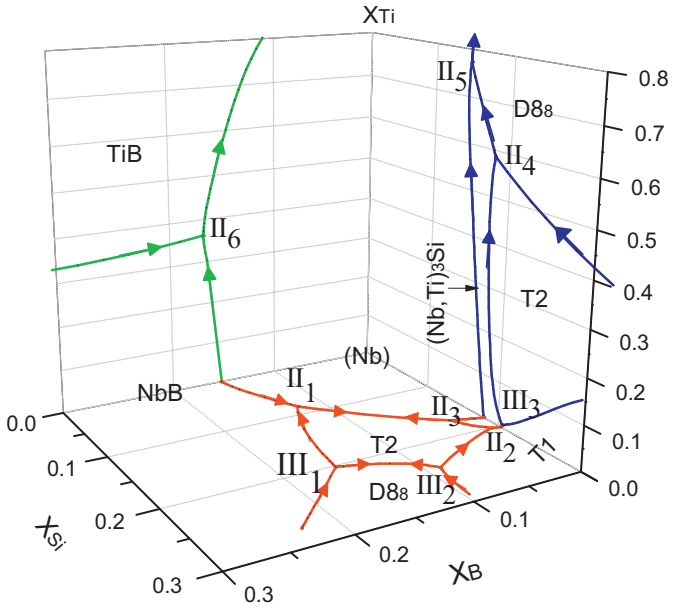

Fig. 1. Calculated liquidus projections of Nb–Si–B, Nb–Ti–Si and Nb–Ti–B in the Nb corner [12–14].

2.2. Nb–Ti–Si

Liang et al. initially assessed the Nb–Ti–Si ternary primarily by direct interpolation based on the descriptions of the constituent binary systems [17]. Yang remodeled this system by considering newly reported experimental data [13]. The calculations from Yang's thermodynamic description yielded good agreements with experimental observations. Recently, Geng et al. modified the thermodynamic description of the binary Nb–Si system based on David's assessment [18], and optimized the Nb–Ti–Si ternary system [19]. Geng's work is consistent with Yang's work in major features. To be consistent with the thermodynamic description of the Nb–Ti–Si–Cr–Hf multicomponent system developed in our research group, the assessment of Yang was accepted in the present work [13].

Fig. 1 (the back-right face) shows the calculated liquidus projection of the Nb–Ti–Si system by Yang [13]. Since α-Nb_5Si_3, β-Nb_5Si_3 and Ti_5Si_3 in the Nb–Ti–Si ternary have the same crystal structure as T2, T1 and $D8_8$ in the Nb–Si–B ternary, respectively, they were modeled as the same phases in the quaternary system, and the same notations of these phases as those in Nb–Si–B were adopted. Two Class-II invariant reactions (II_4 and II_5) and one Class-III invariant reaction (III_3) exist in the Nb-rich region of the Nb–Ti–Si liquidus projection. The invariant reaction at II_4 in Fig. 1 is L + T2 → $D8_8$ + $(Nb,Ti)_3Si$. The calculated temperature and liquid composition of this reaction are 1615 °C and Nb–55.6Ti–18.3Si, respectively. The invariant reaction at II_5 in Fig. 1 is L + $(Nb,Ti)_3Si$ → Nbss + $D8_8$ with calculated temperature and composition being 1352 °C and Nb–76.6Ti–14.5Si, respectively. All alloy compositions in this paper are in atomic percent unless otherwise stated. The calculated results agree well with the experimental measurements [20]. Symbol III_3 in Fig. 1 denotes the invariant reaction L + T2 + T1 → $(Nb,Ti)_3Si$ with calculated temperature and composition being 1974 °C and Nb–0.6Ti–20.4Si, respectively, which is very close to the peritectic reaction L + T1 → Nb_3Si in the Nb–Si binary. Yang also performed solidification simulation for alloys in this region [13]. The simulation results can well account for the experimentally observed as-cast microstructure.

2.3. Nb–Ti–B

Witusiewicz et al. and Nakama et al. performed separate thermodynamic assessment for the Nb–Ti–B ternary [21,22], and achieved reasonable agreements between the calculated and experimental results regarding 1400 °C isothermal section, vertical sections of $Ti_{99.5}B_{0.5}$–$Nb_{98}B_2$ and $Ti_{92.5}B_{7.5}$–$Nb_{92.5}B_{7.5}$, liquidus projection and solidus projection. Nakama et al. also did first-principle calculations to estimate the formation enthalpy calculations of Nb_3B_2, NbB, TiB, Nb_5B_6, $(Nb,Ti)_3B_4$ and $(Nb,Ti)B_2$ with the compositional range along the Nb–Ti direction [22].

Witusiewicz et al. and Pecanha et al. have developed the thermodynamic modeling of the Nb–B binary system and calculated similar phase diagrams in the Nb-rich corner in Nb–Ti–B system [21,23]. Pecanha et al. used the more reasonable $(\mathbf{Nb},Va)_1(\mathbf{B},Va)_2$ model to describe NbB_2 [23], while $(\mathbf{Nb},B)_1(\mathbf{B},Nb)_2$ was used in Witusiewicz et al.'s work [21]. The thermodynamic description modeled by Pecanha et al. was thus used in the modeling work of the Nb–Si–B system [12]. For the Ti–B system, thermodynamic descriptions have been reported by Batzner, Witusiewicz et al. and Nakama et al. [21,22,24]. The difference between their modeling works is about TiB_2. Batzner treated TiB_2 as a stoichiometric compound [24], while Witusiewicz et al. and Nakama et al. took into account the solubility range of 65.2–67.6 at.% B for TiB_2 [21,22]. This difference about TiB_2 has less effect on the phase equilibria in Nb-rich corner and the thermodynamic parameters of binary phases for Ti–B from Batzner have been taken in the Ti–Si–B system [15]. To construct a compatible thermodynamic description for the multi-component Nb–Si alloys, we developed the thermodynamic description of the Nb–Ti–B ternary [14], based on the thermodynamic parameters in Nb–B, Ti–B and Nb–Ti systems from Pecanha et al., Batzner and Kumar et al., respectively [23–25]. The thermodynamic descriptions from Witusiewicz et al. and Nakama et al. and our work agreed with each other and could reproduce the available experimental data of Nb–Ti–B [14,21,22].

In the region with the B concentration up to 30 at.%, there is one Class II invariant reaction. This phase transition is L + NbB → Nbss + TiB, denoted by II_6 in Fig. 1 (the back-left face). A eutectic line extends from L → Nbss + NbB in the Nb–B binary to L → Nbss + TiB in the Ti–B binary. The calculated liquid composition and temperature of this reaction are Nb–36.3Ti–16.8B and 1866 °C, respectively. They are in reasonably good agreement with the estimated liquid composition Nb–39Ti–13B and the experimentally measured temperature 1790 °C as such a high temperature reaction [26]. The developed thermodynamic description for Nb–Ti–B is considered reliable to provide a very useful basis for interpolation into the Nb–Ti–Si–B quaternary system.

2.4. Ti–Si–B

Yang et al. developed the thermodynamic description of the Ti–Si–B system based on the available experimental data [15]. Since the Ti–Si–B ternary is far away from the Nb-rich region and has less effect on the liquidus surface in this region, it is not introduced here. A detailed description can be found in the original work [15].

Based on thermodynamic descriptions of the four constituent ternaries, Gibbs energy functions of phases in the Nb-rich Nb–Ti–Si–B were obtained through interpolation [12–15], and liquidus projection then can be calculated from these functions. The compositions of alloys were selected from the calculated liquidus projection for further experimental verification of the model.

3. Experimental procedures

Seven alloys were selected for experimental investigation. Table 2 lists the nominal composition of each alloy. All of the starting materials used in this work are high purity elements: 99.97% Nb foil, 99.95% Nb slugs, 99.995% Ti slugs, 99.9999% Si lumps and 99.5% B crystals. Button ingots, each about 6 g, were prepared by non-consumable tungsten electrode arc melting in a water-cooled copper crucible in an ultrahigh purity argon atmosphere (99.998% Ar). Before arc melting, each component was accurately weighed and the Nb slugs, Ti slugs, Si lumps and B crystals were wrapped by the Nb foil to reduce the vaporization of Ti, Si and B at high temperatures. Each alloy was melted and flipped five times to promote complete mixing and melting. Only the ingots with a weight loss of less than 0.5 wt.% were chosen for further investigations, and the actual compositions were considered very close to the nominal compositions. The microstructure analysis procedures for the as-cast samples are similar as for the annealed samples, which have been described in more detail previously [6].

Table 2
The nominal compositions of the investigated alloys.

No.	Nominal composition (at.%)
1#	Nb–12Ti–16Si–16B
2#	Nb–23.5Ti–16Si–10B
4#	Nb–4.5Ti–16Si–14B
5#	Nb–6Ti–16Si–12B
6#	Nb–14.5Ti–16Si–12B
7#	Nb–18Ti–16Si–10B
3#	Nb–20Ti–16Si–1.5B

4. Thermodynamic modeling

Microstructure characterization results of these seven alloys suggested that solubilities of Nb_3B_2 and T2 are extensive. In the present work, the sublattice models of $(\mathbf{Nb},Ti)_3(\mathbf{B},Si)_2$ and $(\mathbf{Nb},Ti)_5(\mathbf{Si},B)_3$ are chosen for Nb_3B_2 and T2, respectively, to satisfactorily account for their homogeneity ranges in the quaternary space. Thermodynamic descriptions for the remaining phases were obtained through interpolation [12–15]. The thermodynamic modeling parameters obtained in this work were optimized by incorporating the experimental results from annealed samples, as shown in Table 3. All the phase diagram calculation and model parameter optimization were carried out in Pandat [27]. The comparison between the calculated phase equilibria at 1500 °C and the experimental observation from annealed samples has been published elsewhere [6]. The experimental information from as-cast microstructure was not used for the optimization, but for comparison and verification with the calculated liquidus projection.

5. Results and discussion

Microstructural characterization results from as-cast alloys, which provided much information on the liquid–solid phase equilibria, together with the calculated results, are now discussed and presented below.

5.1. Liquid–solid phase equilibria in the Nb-rich region

As shown in Fig. 1, the primary solidification regions in the Nb-rich corner of the Nb–Ti–Si–B system are bounded by those phases from the constituent binaries and ternaries: Nbss, T2, T1, $D8_8$,

Table 3
The parameters obtained for T2 and Nb_3B_2 in this study.

Phase name	Parameters (in J/mol)
T2	${}^{\circ}G^{T2}_{Ti:B} = 0.625\,{}^{\circ}G^{HCP\_A3}_{Ti} + 0.375\,{}^{\circ}G^{Beta\text{-}rhomb\_B}_{B} - 21{,}007.4$ $L^0_{Ti:B,Si} = 47{,}032.3$ $L^1_{Ti:B,Si} = -9096.19$ $L^0_{Nb,Ti:B} = -85{,}036.5$
Nb_3B_2	${}^{\circ}G^{Nb_3B_2}_{Nb:Si} = 0.6\,{}^{\circ}G^{BCC\_A2}_{Nb} + 0.4\,{}^{\circ}G^{Diamond}_{Si} - 34{,}615.2$ ${}^{\circ}G^{Nb_3B_2}_{Ti:Si} = 0.6\,{}^{\circ}G^{HCP\_A3}_{Ti} + 0.4\,{}^{\circ}G^{Diamond}_{Si} - 10{,}039.44$ $L^0_{Ti:B,Si} = 7468.08$ $L^0_{Nb,Ti:Si} = -98{,}431.6$ $L^1_{Nb,Ti:Si} = -13{,}6431.6$

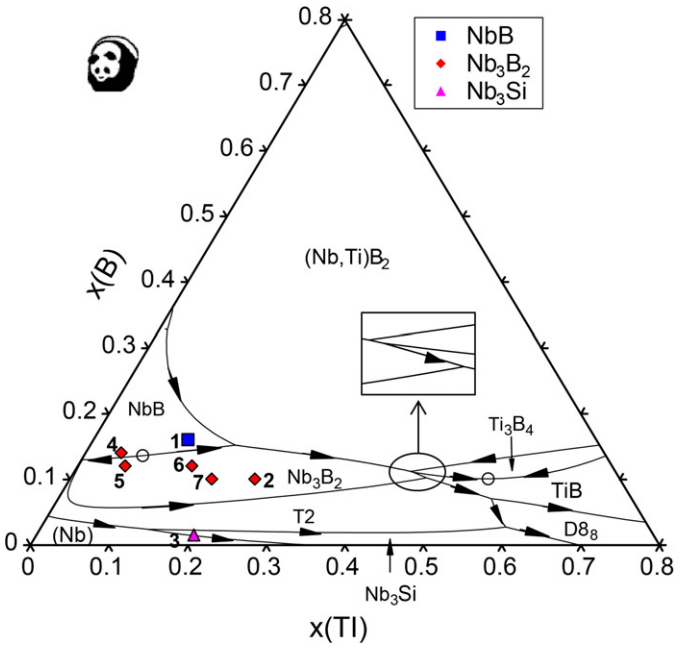

Fig. 2. Calculated 2D liquidus section of Nb–Ti–Si–B (X_{Si} = 16 at.%) and the experimentally observed primary solidification regions.

$(Nb,Ti)_3Si$, NbB and TiB. In the as-cast microstructure of investigated alloys, Nb_3B_2 phase was observed in addition to these phases. Nb_3B_2 is formed from the peritectoid reaction NbB + Nbss → Nb_3B_2 at 2072 °C in the Nb–B binary [23], and there is no primary solidification regions of Nb_3B_2 in the constitute binaries and ternaries. This study suggests that Ti and Si additions increase the stability of Nb_3B_2, thus the primary region of Nb_3B_2 appears in the Nb–Ti–Si–B quaternary.

The liquid–solid phase equilibria of a ternary are normally visualized through a liquidus projection on the composition plane. In quaternary, the composition space is three-dimensional, as shown in Fig. 1. The visualization of liquidus projection in a three-dimensional space is difficult. Therefore, composition of one component will be fixed so that the liquidus projection could be visualized in a two-dimensional diagram. A two-dimensional (2D) section of liquidus projection consists of univariant lines of three-phase equilibria between liquid and other two solid phases [28]. It is useful not only for easy visualization but also for retaining important information about the multicomponent liquidus surface [28]. Fig. 2 shows the calculated 2D section of the Nb–Ti–Si–B liquidus projection with Si fixed at 16 at.%. The lines in Fig. 2 are univariant lines of three-phase equilibria, and the areas are nine primary solidification regions: Nbss, T2, Nb_3Si, Nb_3B_2, NbB, $(Nb,Ti)B_2$, Ti_3B_4, TiB and $D8_8$. Besides these phases originated from constituent binary and ternaries, the primary Nb_3B_2 region is shown in this 2D section. The symbols denote the bulk compositions of the investigated alloys located in different primary phase regions. The calculated primary solidification regions for the investigated alloys are in good agreement with experimental observations. It is worth noting that the composition of liquid is varying during solidification process. Fig. 2 is a section of the liquidus surface with Si fixed at 16 at.%, so the solidification path of an alloy cannot been visualized directly in Fig. 2.

Fig. 3(a) and (b) shows the calculated Nb–Ti–Si–B liquidus projections at 4 at.% B and 7 at.% B, respectively. As seen in Fig. 1 (the Nb–Ti–Si face), there is no direct eutectic reaction between Nbss and T2 in the Nb–Ti–Si ternary. However, with the addition of 4 at.% B, direct eutectic solidification occurs between Nbss and T2 in the Nb-rich Nb–Ti–Si–B liquidus projection. The Nb_3Si primary solidification region is greatly reduced. With more addition of B (i.e., 7 at.%), the Nb_3B_2 primary solidification region comes in between Nbss and α-Nb_5Si_3(T2) and the Nb_3Si primary phase region completely disappears in this 2D section of liquidus projection. These calculations suggest that the B additions destabilize Nb_3Si primary solidification and stabilize Nb_3B_2 primary solidification.

5.2. As-cast microstructures

Solidification paths substantially determine the final solidification microstructure and the subsequently annealed microstructures, and are essential for material design and processing. Two simple models, equilibrium solidification and Scheil solidification have been integrated into Pandat for calculating solidification paths [27]. The cooling speed of the chilled copper-mold cast in this study is rather fast, therefore, the experimental results from as-cast microstructure were compared with the Scheil-model predicted solidification paths. Details are given below.

5.2.1. NbB primary solidification

The low mag. and high mag. BSE images of the as-cast microstructure of Alloy #1 (Nb–12Ti–16Si–16B) are shown in Fig. 4(a) and (b), respectively. The observed phases are dark gray NbB primary phase, large amount of a medium gray phase Nb_3B_2, and the eutectic-like microstructure of Nbss + T2. The simulated solidification path in Fig. 4(c) predicts the primary solidification phase as NbB, then the liquid composition transverses the peritectic ridge of L + NbB → Nb_3B_2, and gets into the primary solidification of Nb_3B_2, in which Nb_3B_2 forms until the liquid composition reaches the eutectic of L → Nb_3B_2 + T2. After the solidification of T2, a variety of eutectic reactions L → Nbss + T2, L → Nbss + T2 + Nb_3Si, L → Nbss + Nb_3Si + Nb_3B_2 and L → Nbss + Nb_3Si + TiB were predicted in sequence. The calculated mole fraction of T2 in the L → Nb_3B_2 + T2 eutectic and the L → T2 stage is 4.0% and 1.2% respectively, so neither the Nb_3B_2 + T2 eutectic nor the primary T2 could be clearly observed in the as-cast microstructure due to their small amount. The predicted three ternary eutectic reactions L → Nbss + T2 + Nb_3Si, L → Nbss + Nb_3Si + Nb_3B_2 and L → Nbss + Nb_3Si + TiB have small mole fractions of 0.4%, 2.9% and 2.3%, respectively. The predicted terminal ternary eutectic reactions cannot be observed in the as-cast microstructure, which is probably due to their small amount or that the actual cooling conditions were different from the Scheil model so that the terminal reactions did not happen. It can be seen in Fig. 4, the experimentally observed phases are well predictable by the simulated Scheil solidification path.

The calculated results using Scheil model can give the element partitioning of the phase from beginning to the end. Table 4 lists the calculated element partitioning in Nb_3B_2 involving only the L → Nb_3B_2 solidification stage of Alloy #1. It can be concluded that the concentrations of Ti and Si in Nb_3B_2 increase during the primary solidification stage of L → Nb_3B_2. Based on EPMA measurements, the average composition of primary Nb_3B_2 was Nb–7.3Ti–16.5Si–24.8B. Considering the experimental uncertainty and the difference between the real situation and the assumptions in Scheil model, the calculated results can be considered to reproduce the experimental data reasonably.

5.2.2. Nb_3B_2 primary solidification

Fig. 5(a) and (b) shows the low mag. and high mag. BSE images of Alloy #2 (Nb–23.5Ti–16Si–10B) respectively. The observed microstructure consists of primary gray Nb_3B_2 phase, a small amount of T2 on the edge of Nb_3B_2 and a fine interdendritic Nbss + T2 eutectic structure. The calculated solidification path of Alloy #2 in Fig. 5(c) starts with the Nb_3B_2 primary solidification, then the liquid composition reaches the eutectic of

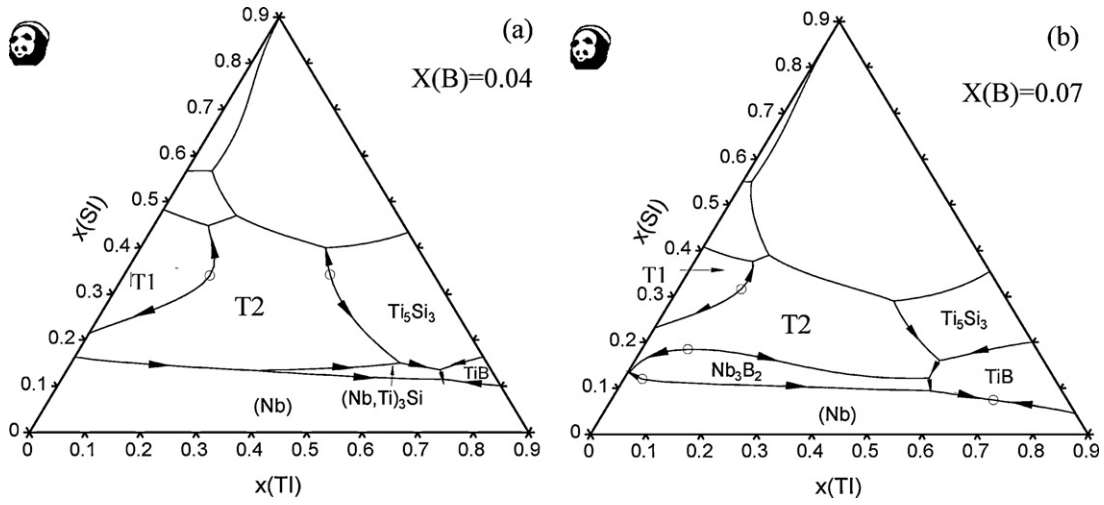

Fig. 3. Calculated 2D liquidus sections of (a) Nb–Ti–Si–B (X_B = 4 at.%) and (b) Nb–Ti–Si–B (X_B = 7 at.%).

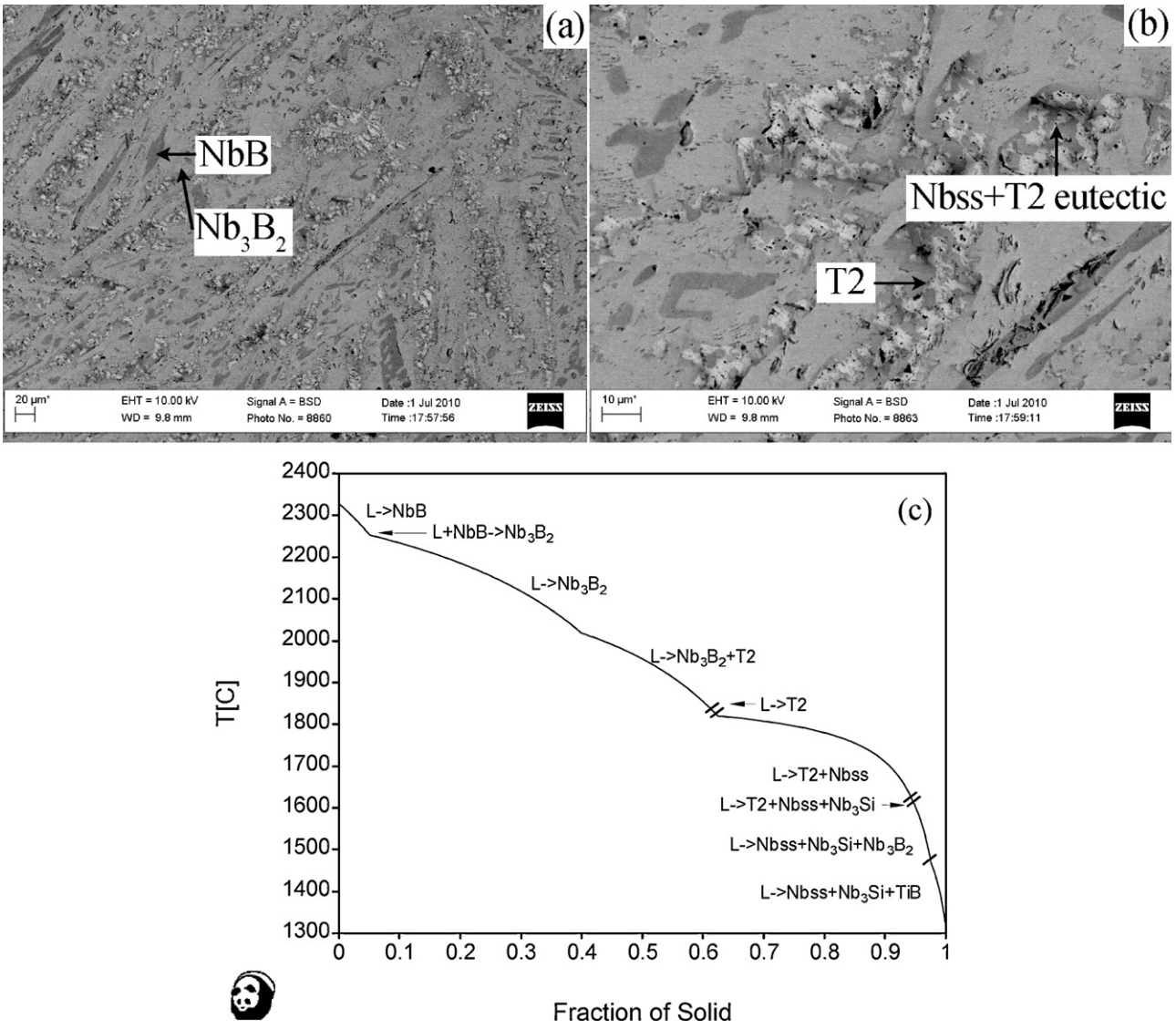

Fig. 4. (a) A low mag. BSE image, (b) a high mag. BSE image of Alloy #1 and (c) calculated Scheil solidification path of Alloy #1.

Table 4
Comparisons between the calculated results and EPMA measurements in dominate or primary phase for the investigated alloys[a].

No.	Phase		Nb	Ti	Si	B
1#	Nb_3B_2	Calc	50.7–49.7	9.2–10.2	10.6–14.8	29.3–25.2
		Exp	51.2	7.3	16.5	24.8
2#	Nb_3B_2	Calc	49.3–48.8	10.6–11.1	13.4–15.0	26.5–25.0
		Exp	47.8	11.8	15.9	24.3
3#	Nb_3Si	Calc	62.1–12.8	12.9–62.2	25	0
		Exp	48.6	25.65	23.4	1.9

[a] The calculated results using Scheil model ("Calc": at.%) give the element partitioning from beginning to the end involving only primary phase solidification stage. "Exp" gives the average phase compositions measured by EPMA (at.%)..

$L \rightarrow Nb_3B_2 + T2$. Then, a small amount of T2 is solidified, and the eutectic of Nbss + T2 was predicted. Finally a variety of ternary eutectics Nbss + T2 + Nb_3Si, Nbss + Nb_3Si + Nb_3B_2, Nbss + Nb_3Si + TiB and Nbss + TiB + $D8_8$ were solidified subsequently, with the calculated mole fractions of 0.2%, 16.7%, 13.3% and 1.1%, respectively. The predicted terminal ternary eutectic reactions cannot be observed in the as-cast microstructure again for the same reason as we discussed for Alloy #1. The observed microstructure in Figs. 5(a) and (b) is in reasonable agreement with the simulated solidification path in Fig. 5(c).

As compared in a similar way for Alloy #1 in Table 4, the calculated compositional range for primary Nb_3B_2 in Alloy #2 well accounted the EPMA determined results. Alloys #4, #5, #6 and #7 have similar microstructures as that of Alloy #2, and are all from Nb_3B_2 primary phase region. They are not discussed in detail here.

5.2.3. Nb_3Si primary phase

The low mag. and high mag. BSE images of the as-cast microstructure of Alloy #3 (Nb–20Ti–16Si–1.5B) are shown in Fig. 6(a) and (b), respectively. It consists of primary faceted

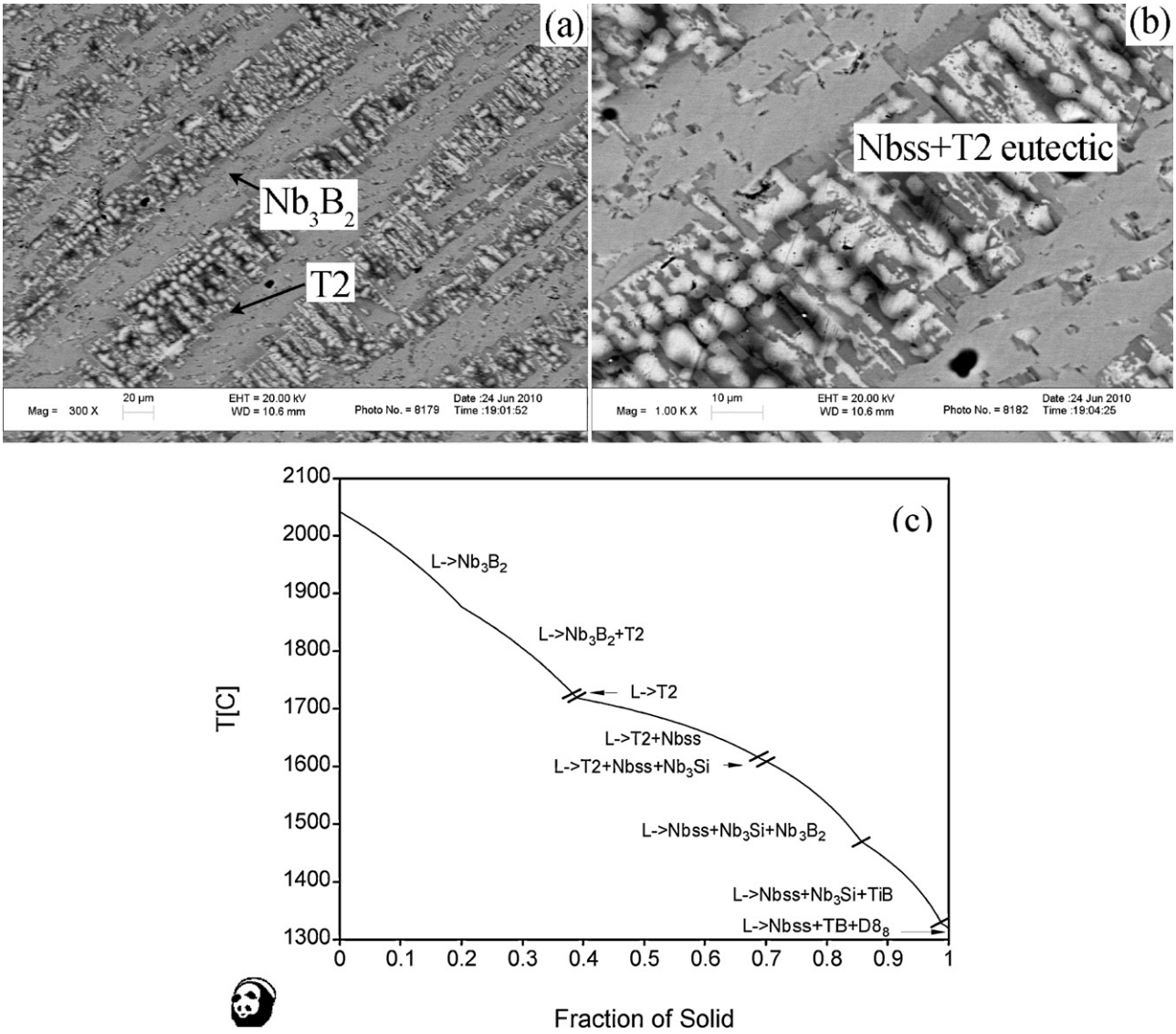

Fig. 5. (a) A low mag. BSE image, (b) a high mag. BSE image of Alloy #2 and (c) calculated Scheil solidification path of Alloy #2.

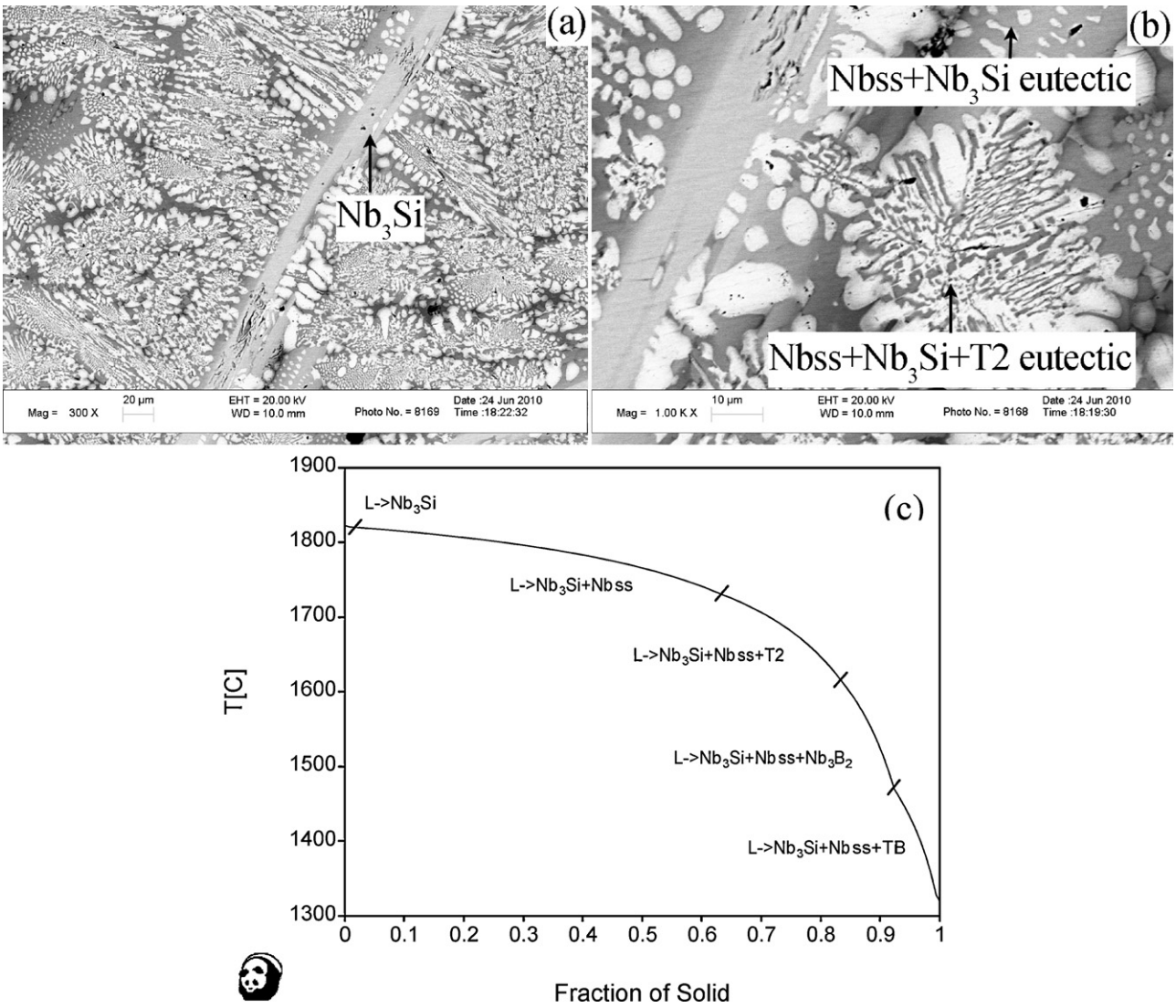

Fig. 6. (a) A low mag. BSE image, (b) a high mag. BSE image of Alloy #3 and (c) calculated Scheil solidification path of Alloy #3.

Nb_3Si phase, binary Nbss + Nb_3Si and fine ternary Nbss + Nb_3Si + T2 eutectic-like microstructures. In the ternary eutectic, the grey Nb_3Si phase and dark grey T2 phase have the compositions of Nb–14.4Ti–23.9Si–1.9B and Nb–18.3Ti–30.8Si–6.3B, respectively, based on EPMA measurements. Fig. 6(c) shows the simulated solidification path of Alloy #3, the beginning stage of the simulated solidification path is the Nb_3Si primary solidification, followed first by the Nbss + Nb_3Si two phase eutectic and then L → Nbss + Nb_3Si + T2, L → Nbss + Nb_3Si + Nb_3B_2 and L → Nbss + Nb_3Si + TiB ternary eutectic reactions. The last two predicted ternary eutectic reactions have small mole fractions of 8.9% and 7.5% respectively. Again, the observed microstructure is consistent with the simulated solidification path. The present study of simple solidification calculations simultaneously validates the reliability of the thermodynamic parameters of this quaternary system and can also give very useful guidance for manufacturing and processing.

As shown in Table 4, the calculated concentration of Ti in Nb_3Si increased from the beginning to the end involving the primary L → Nb_3Si solidification stage. Good agreement was achieved between the calculated and experimental determined compositions for primary Nb_3Si in Alloy #3.

6. Conclusions

The liquid–solid phase equilibria in Nb-rich corner of the Nb–Ti–Si–B system have been proposed for the first time using the CALPHAD approach. Model parameters are required for Nb_3B_2 and T2 in the quaternary system, due to the rather strong quaternary interactions, while thermodynamic descriptions for the remaining phases were obtained from interpolation. The proposed liquidus surface of the Nb-rich Nb–Ti–Si–B system is associated with eight primary solidification regions: Nbss, T2, T1, $D8_8$, $(Nb,Ti)_3Si$, NbB, TiB and Nb_3B_2. Nb_3B_2 was stabilized in the quaternary space due to the substitution elements of Ti and Si, while other phases were from constitute ternaries.

The calculated primary solidification regions in Nb-rich corner are in accordance with the observed phases presented in the as-cast microstructure of seven alloys. The comparisons between the observed phases presented in the as-cast microstructure of the seven alloys with those predicted from the Scheil simulation were performed and good agreements are achieved. This suggests that the topological features of the currently proposed liquidus surface in the Nb-rich region of the Nb–Ti–Si–B system are correct.

The calculated phase diagram in this work can serve as a guide to design alloy compositions for future experimental study.

Acknowledgements

The authors would like to thank CompuTherm LLC for their support of using Pandat program, and Prof. Y.A. Chang (University of Wisconsin-Madison) for experimental support and discussion.

References

[1] B.P. Bewlay, H.A. Lipsitt, M.R. Jackson, W.J. Reeder, J.A. Sutliff, Mater. Sci. Eng. A 192/193 (1995) 534–543.
[2] B.P. Bewlay, M.R. Jackson, H.A. Lipsitt, Metall. Mater. Trans. A 27A (1996) 3801–3807.
[3] N. Sekido, Y. Kimura, S. Miura, F-G. Wei, Y. Mishima, J. Alloys Compd. 425 (2006) 223–229.
[4] Y.-H. Liu, A.J. Thom, M.J. Kramer, M. Akinc, Processing and oxidation behavior of Nb–Si–B intermetallics, 2004, http://www.osti.gov/bridge/purl.cover.jsp?purl=/832901-W18YMO/native/.
[5] G. Rodrigues, C.A. Nunesr, P.A. Suzuki, G.C. Coelho, Intermetallics 12 (2004) 181–188.
[6] Z-P. Sun, Y. Yang, X-P. Guo, C. Zhang, Y.A. Chang, J. Phase Equilibr. Diffus. 32 (2011) 407–411.
[7] B.P. Bewlay, Y. Yang, R.L. Casey, M.R. Jackson, Y.A. Chang, Intermetallics 17 (2009) 120–127.
[8] Y. Yang, B.P. Bewlay, Y.A. Chang, J. Phase Equilibr. Diffus. 28 (1) (2007) 107–114.
[9] H-S. Guo, X-P. Guo, Scripta Mater. 64 (2011) 637–640.
[10] Y.A. Chang, S-L. Chen, F. Zhang, X-Y Yan, F-Y Xie, R. Schmid-Fetzerd, W.A. Oates, Prog. Mater. Sci. 49 (2004) 313–345.
[11] Y.A. Chang, Y. Yang, in: J-C. Zhao (Ed.), Application of Computational Thermodynamics to Rapidly Determine Multicomponent Phase Diagrams, Methods for Phase Diagram Determination, Elsevier Science, 2007.
[12] Z.-P. Sun, Y. Yang, X-P. Guo, C. Zhang, Y.A. Chang, Intermetallics 19 (2011) 26–34.
[13] Y. Yang, Thermodynamic Database of Nb Silicide based Alloys, CompuTherm LLC, 437S, Yellowstone Dr., Suite 217, Madison, WI 53719, 2005.
[14] Z.-P. Sun, Y. Yang, Private Communication, CompuTherm LLC, 437S, Yellowstone Dr., Suite 217, Madison, WI 53719, 2010.
[15] Y. Yang, Y.A. Chang, L. Tan, Intermetallics 13 (2005) 1110–1115.
[16] D.M.P. Junior, C.A. Nunes, G.C. Coelho, F. Ferreira, Intermetallics 11 (2003) 251–255.
[17] H. Liang, Y.A. Chang, Intermetallics 7 (1999) 561–570.
[18] N. David, Y. Cartigny, T. Belmonte, J.M. Fiorani, M. Vilasi, Intermetallics 14 (2006) 464–473.
[19] T. Geng, C.-R. Li, J. Bao, X-Q. Zhao, Z.-M. Du, C.-P. Guo, Intermetallics 17 (2009) 343–357.
[20] B.P. Bewlay, M.R. Jackson, H.A. Lipsitt, J. Phase Equilibr. Diffus. 18 (3) (1997) 264–278.
[21] V.T. Witusiewicz, A.A. Bondar, U. Hecht, S. Rex, T.Ya. Velikanova, J. Alloys Compd. 456 (2008) 143–150.
[22] Y. Nakama, H. Ohtani, M. Hasebe, Mater. Trans. 50 (5) (2009) 984–993.
[23] R.M. Pecanha, F. Ferreira, G.C. Coelho, C.A. Nunes, B. Sundman, Intermetallics 15 (2007) 999–1005.
[24] C. Batzner, Thesis, Max Planck Institut-PML, Stuttgart, FRG, 1994.
[25] K.C.H. Kumar, P. Wollants, L. Delaey, CALPHAD 18 (1) (1994) 71–79.
[26] D.B. Borysov, L.V. Artyukh, A.A. Bondar, P.S. Martsenyuk, A.V. Samelyuk, N.I. Tsyganenko, O.S. Fomichov, T.Ya. Velikanova, Poroshkovaya Metallurgiya 1–2 (2007) 72–87 (in Russian).
[27] Pandat, Software Package for Multi-component Phase Diagram Calculation, CompuTherm LLC, 437 S. Yellowstone Dr, Madison, WI 53719, USA, 1999.
[28] S.-L. Chen, Y. Yang, W.-S. Cao, B.P. Bewlay, K.-C. Chou, Y.A. Chang, J. Phase Equilibr. Diffus. 29 (5) (2008) 390–397.